

# Conformation of a Trimannoside Bound to Mannose-Binding Protein by Nuclear Magnetic Resonance and Molecular Dynamics Simulations

Eric W. Sayers\* and James H. Prestegard†

\*Department of Pharmacology, Yale University, New Haven, Connecticut 06510 and †Complex Carbohydrate Research Center, Athens, Georgia 30603 USA

**ABSTRACT** A model of the carbohydrate recognition domain of the serum form of mannose-binding protein (MBP) from rat complexed with methyl 3,6-di-O-( $\alpha$ -D-mannopyranosyl)- $\alpha$ -D-mannopyranoside is presented. Allowed conformations for the bound sugar were derived from simulated annealing protocols incorporating distance restraints computed from transferred NOESY spectra. The resulting sugar conformations were then modeled into the MBP binding site, and these models of the complex were refined using molecular dynamics (MD) simulations in the presence of solvent water. These studies indicate that only one of the two major conformations of the  $\alpha(1\rightarrow6)$  linkage found in solution is significantly populated in the bound state ( $\omega = 60^\circ$ ), whereas the  $\alpha(1\rightarrow3)$  linkage samples at least two states, similar to its behavior in free solution. The bound conformation allows direct hydrogen bonds to form between the sugar and K182 of MBP, in addition to other water-mediated hydrogen bonds. Estimates of binding constants of candidate complexes based on changes in solvent-accessible surface areas upon binding support the NMR and MD results. These estimates further suggest that the enthalpic gains of the additional sugar-MBP interactions in a trisaccharide as opposed to a monosaccharide are offset by entropic penalties, offering an explanation for previous binding data.

## INTRODUCTION

Mannose-binding protein (MBP) is a member of the collectin family of proteins, a group of mammalian lectins that contain a common calcium-dependent (C-type) carbohydrate recognition domain (CRD) (Drickamer, 1988, 1993). In addition, collectins typically have a cysteine-rich N-terminus, a collagenous region, and a short  $\alpha$ -helical coiled-coil neck (Hoppe and Reid, 1994a). MBP is also an integral part of the innate immune system (Hoppe and Reid, 1994b; Lu, 1997) and is unique among the collectins in that, after binding to carbohydrates on the surfaces of an invading microorganism, it can directly activate the complement system, leading to the destruction of the pathogen (Gadjeva et al., 2001). In humans, three structural mutations in MBP have been identified in the collagenous region, which, in homozygous individuals, dramatically reduce the serum levels of MBP (Summerfield, 1993; Turner, 1996; Ezekowitz, 1998). Such reduced serum levels of MBP have, in turn, been associated with the common opsonic defect in infants (Super et al., 1989) and vulnerability to infectious diseases (Garred et al., 1995, 1997; Thomas et al., 1996; Summerfield et al., 1997), autoimmune diseases (Davies et al., 1997; Kilpatrick, 1997), and recurrent miscarriage (Turner, 1998). Clearly, knowing the details of the protein-carbohydrate

interactions through which MBP recognizes invading pathogens is critical in understanding the function of this protein.

To date binding studies for MBP have concentrated on the two well-characterized forms of MBP found in rat: MBP-A found in the serum and MBP-C found primarily in the liver (Drickamer et al., 1986). Although both MBP-A and MBP-C bind to simple monosaccharides (D-mannose, N-acetylglucosamine, L-fucose) with similar affinities (Quesenberry et al., 1997), early studies indicated that MBP-C primarily recognizes the core structures of complex oligosaccharides, whereas MBP-A only recognizes the terminal monosaccharides of these structures (Childs et al., 1990). These results were supported by later studies that again found that MBP-C had a higher affinity for oligosaccharides compared to MBP-A. This prompted a proposal that the binding site of MBP-A is compact, interacting only with a single sugar residue, whereas that of MBP-C is more extended (Lee and Lee, 1997; Quesenberry et al., 1997; Lee et al., 1999). Interestingly, other studies have shown that, although MBP-A can activate the complement cascade, MBP-C cannot (Ikeda et al., 1987). Thus, the evidence suggests that the specificity difference between the two forms of MBP may be functionally important, and raises the question of why monosaccharides and oligosaccharides have the same affinity for MBP-A but not MBP-C.

The first structure available for an MBP was that for the isolated MBP-A CRD from rat (Weis et al., 1991a,b); a structure of the same CRD complexed to an oligosaccharide followed (Weis et al., 1992). These structures revealed a binding site organized by a calcium ion, which also directly coordinates the OH3 and OH4 groups of the terminal mannose residue. There are now 22 published crystal structures of rat MBPs; these include MBP-A or MBP-C, their mutants, and various saccharide complexes (Håkansson and

Submitted September 6, 2001 and accepted for publication November 18, 2001.

Dr. Sayers' present address is Molecular Structural Biology Unit, National Institute of Dental and Craniofacial Research, National Institutes of Health, 30 Convent Dr., MSC 4307, Bethesda, MD 20892.

Address reprint requests to James H. Prestegard, Complex Carbohydrate Research Center, 220 Riverbend Rd., Athens, GA 30603-4712. Tel.: 706-542-4401; Fax: 706-542-4412; E-mail: jpresteg@ccrc.uga.edu.

© 2002 by the Biophysical Society

0006-3495/02/05/2683/17 \$2.00

Reid, 2000). In addition, our group recently presented a structure of methyl  $\alpha$ -D-mannopyranoside ( $\alpha$ -Me-Man) bound to MBP-A derived from residual dipolar couplings seen in nuclear magnetic resonance (NMR) data (Bolon et al., 1999; Al-Hashimi et al., 2000). However, most of the ligands in these structures are monosaccharides; indeed, the 1992 structure of Weis and co-workers is still the only structure of a wild-type MBP complexed with an oligosaccharide. No structures have been reported for MBP-C complexed with an oligosaccharide. However, the crystal structure of MBP-C complexed with  $\alpha$ -Me-Man showed that the positions of the OH3 and OH4 groups in the calcium coordination shell were reversed relative to those in the MBP-A complex, effectively rotating the sugar ring by  $180^\circ$  (Ng et al., 1996). As yet it is unclear what role this change in binding geometry plays in determining the ligand specificity of MBP-C. Also, although the 1992 MBP-A/oligosaccharide structure is valuable, the oligosaccharide cross-links two CRDs, a geometry that may impose nonphysiological limits on the carbohydrate conformation. Because the biologically relevant ligands of MBP are thought to be complex oligosaccharides, additional structural information on such complexes should be helpful in characterizing the details of how MBP recognizes these ligands. As a step toward this goal, results of a combined NMR and molecular dynamics (MD) study of a recombinant form of the rat MBP-A CRD (MBP-2) complexed to methyl 3,6-di-O-( $\alpha$ -D-mannopyranosyl)- $\alpha$ -D-mannopyranoside (trimannoside) are presented. This trimannoside is the heart of the common core structure of N-linked oligosaccharides. Our recently published study of the behavior of this trimannoside in free solution (Sayers and Prestegard, 2000) will be used as a starting point in obtaining a model for the bound state of the trimannoside. A comparison of the resulting model to existing structures will reveal possible explanations for the observed binding specificity of MBP-A.

## EXPERIMENTAL PROCEDURES

### Materials

Methyl 3,6-di-O-( $\alpha$ -D-mannopyranosyl)- $\alpha$ -D-mannopyranoside was obtained from BIOMOL Research Labs, Inc. (Plymouth Meeting, PA), and was used without further purification. The ring numbering system used in this work is shown in Fig. 1 along with the nomenclature for the dihedral angles, which were defined according to IUPAC conventions (IUPAC-IUB, 1983):  $\phi = O5(i)-C1(i)-On(i-1)-Cn(i-1)$ ,  $\psi = C1(i)-On(i-1)-Cn(i-1)-C(n-1)(i-1)$ ,  $\omega = O6(i)-C6(i)-C5(i)-C4(i)$ , where (*i*) indicates a given residue and (*n*) a ring position. [ $^{13}C_6$ ]- $\alpha$ -Me-Man was prepared as described previously (Sayers et al., 1998).

### Preparation of plasmid pMBP-2

To eliminate the need for proteolysis of an existing MBP construct to remove an  $\alpha$  helical stem involved in trimerization (Weis et al., 1991a), a new truncated construct was prepared. Oligonucleotide primers used for PCR were prepared in the laboratory of Dr. Alanna Schepartz (Yale

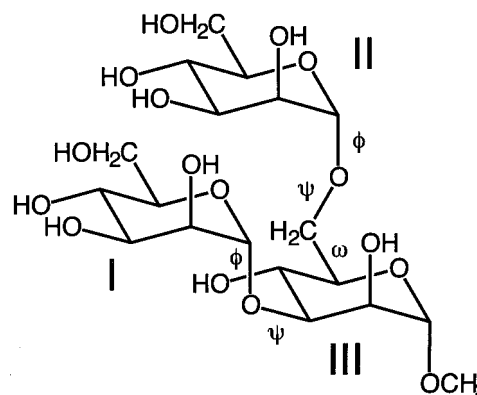


FIGURE 1 Structure of methyl 3,6-di-O-( $\alpha$ -D-mannopyranosyl)- $\alpha$ -D-mannopyranoside. Rings are labeled by roman numerals, and glycosidic dihedral angles are labeled  $\phi$ ,  $\psi$ , and  $\omega$ .

University) by solid phase synthesis. Two primers were used in the present work: primer 5p2 (5'-GCT AAA AAG CAT ATG AAG AAG TTC-3') and primer 3p (5'-GCA CTG GGA TCC TCA GGC TGG-3'). Primer 5p2 introduced an *Nde* I site (underlined) and a start codon that directed protein synthesis to begin at K109 of the MBP-A gene (Drickamer et al., 1986). Primer 3p introduced a *Bam*H I site (underlined) and a stop codon that directed protein synthesis to end at A221, the native C-terminus. The MBP-2 protein thus produced is shorter by two residues than the initially crystallized MBP-A-F2 protein, whose N-terminus was S107 (Weis et al., 1992). PCR reactions were performed using either *Taq* or *Pfu* DNA polymerase, and contained plasmid pIN-IIIompA-2 (Drickamer, 1989) as template and primers 5p2 and 3p. For reactions using *Taq* (*Pfu*) polymerase, 30 (20) cycles were performed with an annealing temperature of  $55^\circ\text{C}$  ( $50^\circ\text{C}$ ). All reactions consistently generated 5–10 ng of a single product of the expected size (368 bp). PCR products were ligated into vector pNoTA using the PRIME PCR CLONER cloning system (5 Prime $\rightarrow$ 3 Prime, Boulder, CO) according to the manufacturer's instructions. After transformation into *Escherichia coli* strain DH5 $\alpha$  cells, plasmids were isolated and screened for the presence of the insert by digestion with *Pvu* II and by fluorescent sequencing. The desired gene was isolated by digestion with *Nde* I and *Bam*H I and then ligated into plasmid pET-3a. After transformation into NovaBlue cells (Novagen, Inc., Madison, WI), plasmids were isolated and screened for the presence of insert by digestion with *Bsm* I, and the fidelity of the final construct, pMBP-2, was confirmed by fluorescent sequencing.

### Preparation of MBP-2

The purification of MBP-2 was performed as described previously (Weis et al., 1991a; Sayers et al., 1998) with the following modifications. During the dialysis step, dialysis tubing with a smaller molecular weight cutoff (3500) was used to prevent loss of the smaller MBP-2 protein. Because MBP-2 was found to precipitate in the absence of  $\text{Ca}^{2+}$ , 1 ml load buffer (1.25 M NaCl, 25 mM Tris-Cl pH 7.8, 25 mM  $\text{CaCl}_2$ ) was added to each fraction immediately after collection to prevent precipitation. Samples of purified MBP-2 were subjected to mass spectrometry, which indicated a molecular weight of  $12659.3 \pm 0.9$ , matching the expected value of 12660.

### NMR sample preparation

Samples containing carbohydrate complexes with MBP-2 were prepared based on previous procedures used for MBP-A-F1' (Sayers et al., 1998). However, because of the instability of MBP-2 in the absence of  $\text{Ca}^{2+}$ , the

procedure was modified as follows. The pooled fractions from the mannose-Sepharose column were dialyzed twice against 100 volumes of 10 mM Tris-Cl pH 7.8 containing 10 mM CaCl<sub>2</sub>, and once against 100 volumes of 1 mM Tris-Cl pH 7.8, also containing 10 mM CaCl<sub>2</sub>. This dialysate (10–15 ml) was then concentrated to 0.5 ml using a CentriPrep 10 concentrator (Amicon, Beverly, MA), and then exchanged into 5 mM [D<sub>11</sub>]-Tris-Cl pH 7.8 containing 10 mM CaCl<sub>2</sub> using a CentriCon 10 concentrator (Amicon). The sample was then lyophilized and redissolved in D<sub>2</sub>O. The desired amount of the carbohydrate stock solution ( $\alpha$ -Me-Man or the trimannoside) was then added to the sample, and the volume was adjusted so that the final buffer concentration was 10 mM [D<sub>11</sub>]-Tris-Cl pH 7.8 containing 20 mM CaCl<sub>2</sub>. Given that MBP-2 exists as a dimer in solution with each monomer having one independent binding site (Weis et al., 1991b, 1992), protein concentrations will be quoted as the molarity of MBP-2 monomers.

## NMR spectroscopy

NMR experiments were performed on either a Varian UNITY spectrometer operating at a proton frequency of 500 MHz and equipped with a Varian triple resonance HCN probe with z gradients, or on a GE Omega spectrometer operating at a proton frequency of 500 MHz and equipped with a Bruker triple-resonance triple-axis gradient probe and an S-17 gradient accessory. After collection, all data were processed using FELIX software (version 95.0, Molecular Simulations, Inc., San Diego, CA). All proton and <sup>13</sup>C chemical shifts are reported relative to internal 3-(trimethylsilyl)-1-propane sulfonic acid, sodium salt as previously outlined (Wishart et al., 1995).

Two-dimensional (2D) <sup>1</sup>H-<sup>13</sup>C HSQC spectra were recorded at 35°C on the Omega 500 as described previously (Sayers et al., 1998). The sample contained 1.5 mM MBP-2 monomers, 1.0 mM  $\alpha$ -Me-Man, and 20 mM CaCl<sub>2</sub> in 250  $\mu$ l D<sub>2</sub>O buffered with 10 mM [D<sub>11</sub>]-Tris-Cl, pH 7.8 in a Shigemi microcell.

Two-dimensional transferred NOESY (TrNOESY) and transferred ROESY (TrROESY) spectra of the MBP-2/trimannoside complex were recorded at 5°C on the Varian 500. The sample contained 2 mM trimannoside, 0.3 mM MBP-2 monomers, and 20 mM CaCl<sub>2</sub> in 0.5 ml D<sub>2</sub>O buffered with 10 mM [D<sub>11</sub>]-Tris-Cl, pH 7.8. TrNOESY spectra were recorded using the standard NOESY pulse sequence (Macura and Ernst, 1980), supplemented by two pulsed field gradients, G1 (1.0 ms, 14 G/cm) and G2 (1.0 ms, 24 G/cm) applied at the beginning and end of the mixing time, respectively, to remove undesired magnetization. TrROESY experiments were also recorded using standard methods (Bothner-By et al., 1984; Bax and Davis, 1985). The spin lock during the ROESY mixing time was implemented as a train of 90° pulses yielding an effective field strength of 5 kHz (Griesinger and Ernst, 1987). For both experiments, solvent suppression was achieved by a 1.5-s presaturation pulse applied at the water frequency. Immediately following this pulse, the proton offset was moved to 5.0 ppm. For the TrNOESY (TrROESY) spectra, a total of 32 (24) scans of 2048 complex points was collected for each of the 256 increments in the indirect time domain. The spectral width in F1 and F2 was 3500 Hz for both experiments, and States-TPPI was used to achieve quadrature in the indirect dimension. The total recycle time was 2.085 s. Each direct dimension free induction decay (FID) was apodized using a Kaiser window before Fourier transformation, whereas each indirect FID was zero-filled to 2048 points and also apodized using a Kaiser window, yielding a 2048  $\times$  2048 matrix. When multiple data sets were collected at different mixing times, the data sets were collected in an interleaved manner.

## Analysis of NMR data

After Fourier transformation, selected one-dimensional (1D) vectors from 2D TrNOESY or TrROESY spectra were first baseline corrected using third-order polynomials, and all peaks were integrated. The integrated

intensities of the auto peaks were extrapolated to  $\tau = 0$  to derive  $M_0$ , the equilibrium magnetization for that spin. The integrated intensities of the cross-relaxation peaks were plotted as fractions of  $M_0$ , and these plots were fit to the approximate magnetization transfer equation given in Eq. 1 using KaleidaGraph 3.0.2 (Synergy Software, Reading, PA):

$$I_c(\tau) = c_1 + c_2\tau \exp(-c_3\tau). \quad (1)$$

In this expression,  $c_1$  is an offset parameter,  $c_2 \propto \sigma$  is the cross-relaxation rate constant, and  $c_3 = 1/T_1$ . Distance restraints were derived from these data using the expression,

$$r_{\text{exp}} = \left( \frac{c_{2\text{ref}}}{c_{2\text{exp}}} \right)^{1/6} r_{\text{ref}}, \quad (2)$$

where  $r_{\text{exp}}$  is the unknown distance between a given spin pair,  $r_{\text{ref}}$  is a known distance between a separate spin pair, and  $c_{2\text{ref}}$  and  $c_{2\text{exp}}$  are the parameters in Eq. 1 corresponding to the two spin pairs. In the present work, the distances and buildup rates of the intraring TrNOESY peaks between the anomeric proton and H2 of each ring were used as  $r_{\text{ref}}$  and  $c_{2\text{ref}}$ , because these distances are fixed and well known. The error in a given distance was derived from the error in the curve fitting of the corresponding buildup rate using standard formulas for propagation of error.

## Computational methods

All minimizations, simulated annealing procedures, and MD simulations were performed using AMBER 4.1 (Pearlman et al., 1995) supplemented by the GLYCAM parameter set (Woods et al., 1995) as previously described (Sayers and Prestegard, 2000). Molecular structures were viewed and manipulated using MidasPlus (Ferrin et al., 1988) and Insight II (v. 98, Molecular Simulations, Inc.). Distance restraints derived from TrNOESY data and torsional restraints locking the pyranose rings into chair conformations were implemented in AMBER in terms of four parameters (r1, r2, r3, r4) as previously described (Sayers and Prestegard, 2000), with the exception that r4 was set to 4.00 Å for positive distance restraints. For all positive restraints, a distance  $r$  was considered to violate the restraint if  $r < r1$  or if  $r > r3 + 0.5$  Å, whereas, for negative restraints, a violation occurred only if  $r < r1$ . Simulated annealing procedures incorporating TrNOESY-derived distance restraints and subsequent minimizations of the free trimannoside were performed in vacuo using the SANDER module of AMBER as previously described (Sayers and Prestegard, 2000).

Models of the trimannoside bound to MBP-2 were constructed starting from the Brookhaven PDB coordinates (entry 2MSB) of the MBP-A/oligosaccharide crystal structure (Weis et al., 1992). The atoms of an MBP-A CRD monomer (except for the N-terminal K109, which had incomplete coordinates) were protonated using the *protonate* module of AMBER. The three calcium ions in the crystal structure were added to this model as separate molecules, and no bonds of any kind were established between the ions and protein atoms. The charge on each calcium was set to +2, and charges on the protein atoms were not adjusted. The Lennard-Jones parameters used for the calcium were  $r^* = 1.60$  Å and  $\epsilon = 0.10$  kcal/mol as included in the 1991 AMBER force field; these parameters were added to the 1994 AMBER force field.

The trimannoside was added to the model by first superimposing the ring atoms of the desired trimannoside residue onto the corresponding atoms of the terminal mannose of the oligosaccharide ligand in the crystal structure. The resulting trimannoside coordinates were then appended to the PDB file of the MBP-2 model described above. Using the LINK and EDIT modules of AMBER, the model of the MBP-2/trimannoside complex was formed and immersed in a bath of TIP3P water. Water molecules were initially placed throughout a region reaching out to 10 Å from MBP-2 and trimannoside atoms with no water oxygen or hydrogen atoms approaching an atom of the complex at distances less than 2.8 and 2.3 Å, respectively. Although the exact size of the resulting water box depended on the

modeled conformation of the trimannoside, simulations typically included ~4700 water molecules in a  $61 \times 56 \times 53$  Å box. The final model was then minimized for 1000 steps in a constant dielectric using the steepest descent method with a 10-Å cutoff for nonbonded interactions.

MD simulations of the minimized model were performed using the SANDER module of AMBER. Simulations were performed under constant pressure conditions in a constant dielectric using a timestep of 1 fs. Scaling factors of 0.2 ps were used in the Berendsen algorithm for the ligand and solvent. The SHAKE algorithm was used to constrain bond lengths, and initial velocities were calculated from a Maxwellian distribution at 10 K. The cutoff for nonbonded interactions was set to 10.0 Å, and the non-bonded pairlist was updated every 25 fs. Each minimized model was initially subjected to two rounds of equilibration. In each round, the system was first heated from 10 to 300 K in 10 ps, then maintained at 300 K for an additional 10 ps, and finally cooled to 10 K in another 10 ps, resulting in a total length of 30 ps for each round. During the first round, all protein and trimannoside atoms were held fixed, allowing only solvent atoms to move. In the second round, the amino-acid side-chain atoms were also allowed to move. For the final simulations, the system was heated from 10 to 300 K in 10 ps, and then maintained at 300 K for 50–100 ps, allowing all atoms to move. No restraints of any kind were used during the final simulations, except in some cases where the distances between the calcium and the OH3 and OH4 oxygens of ring I were restrained (see below). When these restraints were used, they were maintained throughout the final simulation. During the course of the two equilibration runs, coordinates and energy statistics were output every 500 fs, but these data were output every 1000 fs during the final simulation.

Water-accessible surface areas (ASA) were calculated from PDB files generated by the MD simulations using Insight II with a 1.4-Å probe radius. Changes in ASA values upon binding were estimated as the difference between the ASA of the complex and the sum of the ASA of the free molecules, where the free molecules were derived from the PDB file of the complex. Estimates for  $\Delta H$  were derived from changes in polar and apolar ASA values using Eq. 2 from the published report (García-Hernández and Hernández-Arana, 1999), whereas  $T\Delta S_{\text{sol}} (kJ/mol)$  was calculated as  $T(\Delta S_{\text{ap}} + \Delta S_{\text{pol}})$ , where, at 25°C,  $\Delta S_{\text{ap}} = -0.095\Delta ASA_{\text{ap}}$  and  $\Delta S_{\text{pol}} = 0.041\Delta ASA_{\text{pol}}$  (García-Hernández and Hernández-Arana, 1999). Values of  $T\Delta S_{\text{tot}}$  were calculated by summing the following entropy losses for each bond frozen upon complex formation: for carbohydrate bonds,  $-6.4$  J/K-mol (García-Hernández and Hernández-Arana, 1999); for an O–H bond in a water molecule,  $-5.0$  J/K-mol (see below); and for the K182 side chain,  $-26.4$  J/K-mol (Doig and Sternberg, 1995).

## RESULTS

### Collection of distance restraints

In principle, the  $1/r^6$  relationship between the intensity of cross-peaks in NOESY spectra and interproton distances ( $r$ ) allows a straightforward determination of molecular structure. When only the average properties of a molecule in fast exchange between a high population in solution and small population bound to a large protein are observable (TrNOESY spectra), extraction of accurate distance restraints is more complex. Before reliable distance information on a bound ligand conformation can be derived, experimental conditions must be found where spin relaxation processes in the bound state dominate processes in the free state. Qualitatively, the observation of negative cross-peaks in TrNOESY spectra (same phase as the diagonal peaks) is a good indicator of appropriate dominance by the bound state (Clare and Gronenborn, 1982). Initial experiments on

the MBP-2/trimannoside complex were conducted at 35°C using a sugar–protein ratio of 12:1. The resulting peaks were greatly reduced in intensity compared to those observed for the free sugar, but were positive. The sugar–protein ratio was therefore lowered to 6:1 and the temperature was lowered to 15°C, and negative TrNOESY peaks were then observed. However, the frequency of the intense water resonance shifted at the lower temperature to a position that made it degenerate with the II-H1 resonance of the trimannoside. This difficulty was solved by lowering the temperature to 5°C. This latter temperature had an additional advantage in that, at 5°C, NOESY cross-peaks for the free trimannoside essentially vanished ( $\omega\tau_c \sim 1$ ), making contributions from relaxation in the free sugar essentially zero.

Another problem associated with many TrNOESY experiments is the existence of efficient indirect magnetization transfer pathways in the bound state. Interference from such pathways can be detected by comparing 2D TrNOESY spectra to 2D TrROESY spectra where distinctive intensity alterations, or even alternations of signs of cross-peaks, can arise from indirect transfers. Selected 1D vectors extracted at the F1 frequencies of well-resolved spins from two such spectra are displayed in Fig. 2. The spectra were phased so that the diagonal peaks were positive, making the TrNOESY peaks positive and TrROESY peaks that arose from direct interactions negative. Most peaks follow this pattern and show only small relative intensity anomalies. For example, the two peaks at 4.08 and 4.06 ppm in vector I-H1 showing connections to III-H2 and I-H2 were observed in the TrROESY spectra in opposite phase and approximately the same relative intensities as expected for direct connectivities. However, the pathways that produced the peak near 4.02 ppm in vector II-H1 appear to be more complex. Although the peak at 3.98 ppm appears in opposite phase and full intensity in the TrROESY spectrum, the weak peak at 4.02 ppm is nearly absent in this spectrum. The peak at 4.02 ppm is assigned to III-H6R based on strong cross-peaks observed in both TrNOESY and TrROESY spectra between this peak and III-H6S (3.72 ppm). The III-H6S,R methylene protons are very close together, and thus they are prime candidates for an indirect transfer. Given the significant cross-peak at 3.72 ppm, an indirect transfer from II-H1 to III-H6R via II-H6S is a distinct possibility that must be kept in mind as the data are analyzed.

Distance restraints were collected by quantitating the buildup of cross-relaxation observed in 1D vectors of the 2D TrNOESY spectra. To treat the complex III-H3/III-H4 multiplet (vector I-H1), its intensity was divided (80/20) between III-H3 and III-H4 based on appropriate simulations of strongly coupled spin systems (Sayers and Prestegard, 2000). Plots of the TrNOESY cross-peak intensities with best-fit theoretical curves are shown in Fig. 3, and the resulting distance restraints are listed in Table 1. Table 1

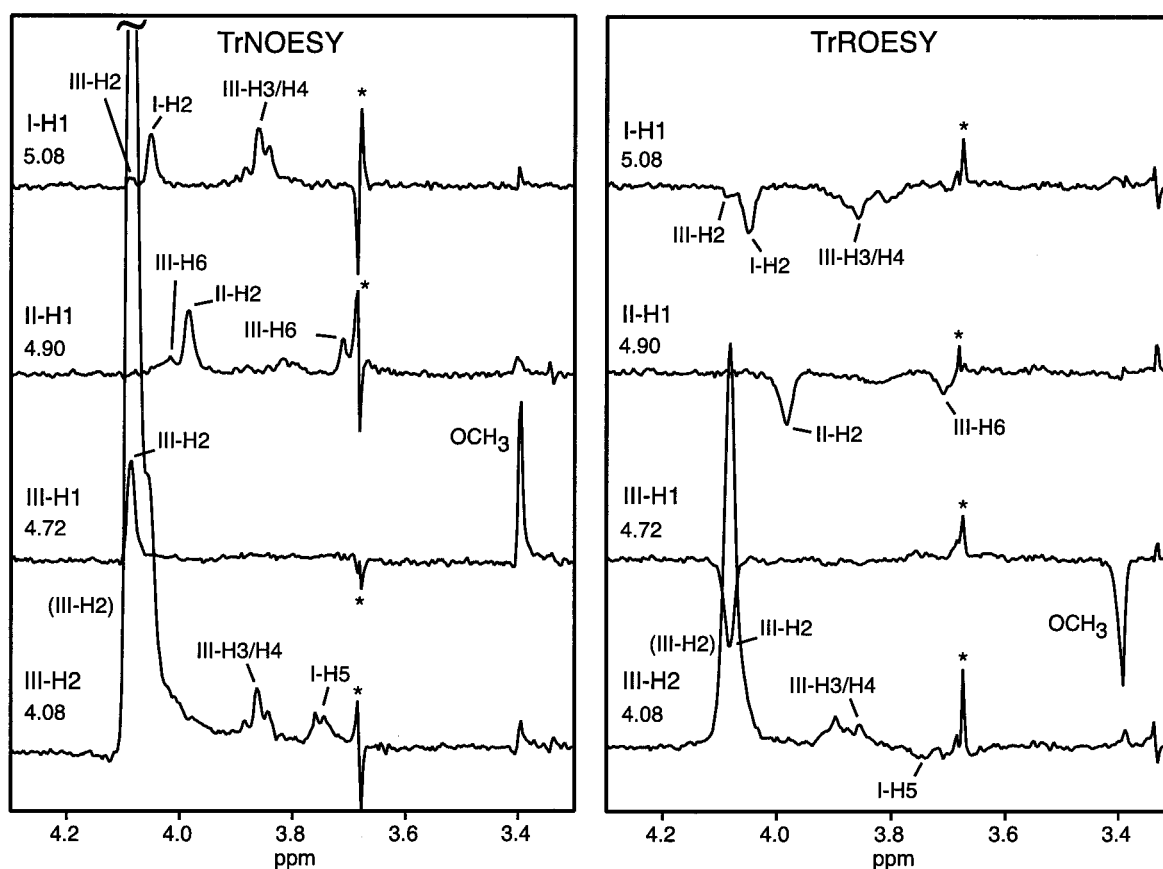


FIGURE 2 One-dimensional vectors extracted from 2D TrNOESY ( $\tau = 250$  ms) and TrROESY ( $\tau = 350$  ms) spectra. Each vector is labeled with its F1 frequency and the corresponding proton, and quantitated cross-relaxation peaks listed in Table 1 are also labeled. The intense peaks at 4.08 ppm for III-H2 are diagonal peaks (sources of magnetization), whereas the sharp, phase-distorted peaks at 3.69 ppm (asterisks) are artifacts resulting from excess Tris buffer. The peaks for III-H1 labeled OCH<sub>3</sub> represent direct contacts between III-H1 and these methyl protons. However, the phase-distorted peaks at 3.40 ppm in the other vectors are artifacts arising from these intense methyl signals.

does not include any restraints between MBP-2 and the trimannoside. This was not surprising, given that the MBP-2 binding site is quite proton poor with respect to nonexchangeable protons within 5 Å of the sugar (Sayers et al., 1998).

### Simulated annealing

The 30 structures of an initial ensemble (MA) calculated using the restraints listed in Table 1 resulted in structures that, after minimization in the absence of restraints, adopted one of five conformations that differed primarily in terms of II–III  $\psi$  and  $\omega$ . Although none of these structures violated any restraints after simulated annealing, all 30 structures minimally violated the restraint on d(I-H1, III-H2) by 0.1–0.4 Å after minimization. More seriously, three conformations contained two proton pairs, (II-H1, III-H4) and (II-H1, III-H5), with internuclear distances of less than 4.0 Å, even though no TrNOESY cross-peaks were observed between these spins. Therefore, these three conformations were likely flawed or populated minimally, and, to eliminate

them from further consideration, additional negative distance restraints on d(II-H1, III-H4) and d(II-H1, III-H5) were introduced in a second round of simulated annealing.

Ensemble MB, an ensemble of 30 structures generated using the modified restraint set, could be divided into four conformations (Table 2), with MB1 and MB2 representing 28 of the 30 structures. Although MB1 is identical to a major solution conformation of the free trimannoside, B2a (Sayers and Prestegard, 2000), the  $\omega = -60^\circ$  state found in MB2 is believed to be populated minimally in pyranose rings of D-mannose or D-glucose due to steric clashes between OH4 and OH6, among other factors (De Bruyn and Anteunis, 1976; Rao and Perlin, 1983). Like MB1, MB3 and MB4 also correspond to conformations identified for the free sugar (B1a and B2b). Interestingly, MB4 departs from MB1 only in the state of the I–III linkage,  $(\phi, \psi) = (90^\circ, -60^\circ)$ , and was the only structure that did not violate the d(I-H1, III-H2) restraint in ensemble MB, a feature that can be traced to the alternate state of the I–III linkage. Finally, conformation MB3 differs from MB1 and MB2 only at II–III  $\omega$ .

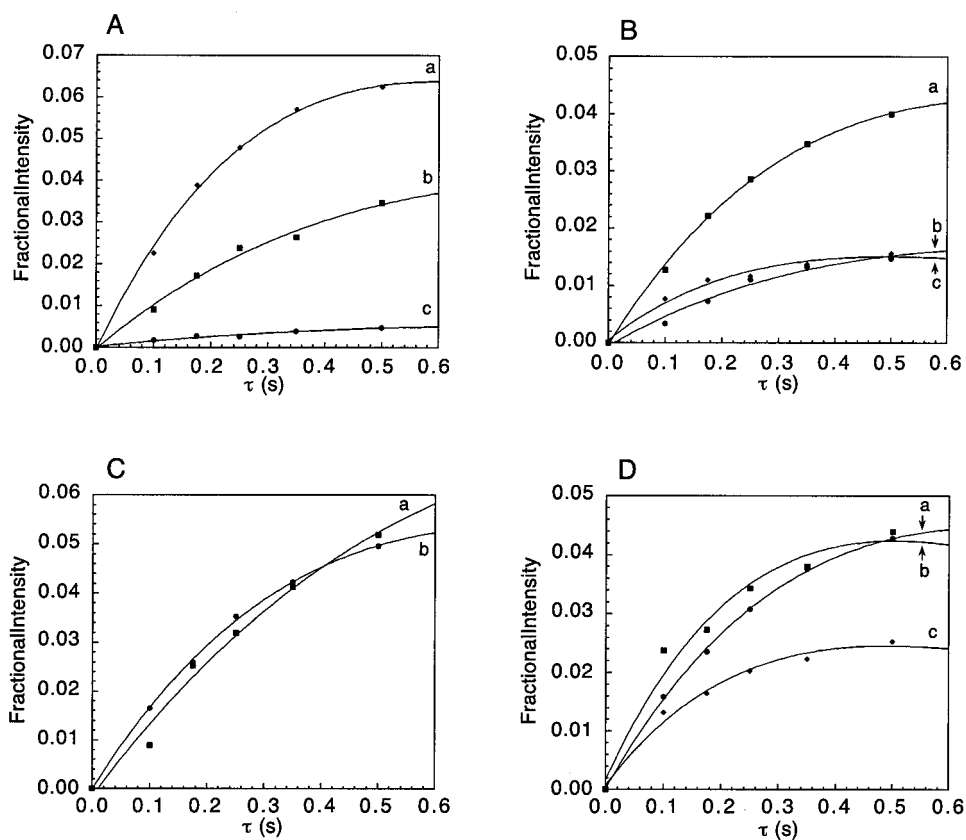


FIGURE 3 Buildup curves obtained from TrNOESY experiments. All intensities are reported as fractional intensities of the auto peak of the inverted spin at  $\tau = 0$ . (A)  $F1 = 5.09$  ppm (I-H1). Intensities of cross-peaks to (a) III-H3/III-H4, (b) I-H2, and (c) III-H2. (B)  $F1 = 4.90$  ppm (II-H1). Intensities of cross-peaks to (a) II-H2, (b) III-H6R, and (c) III-H6S. (C)  $F1 = 4.72$  ppm (III-H1). Intensities of cross-peaks to (a) III-H2, and (b)  $\text{OCH}_3$ . (D)  $F1 = 4.08$  ppm (III-H2). Intensities of cross-peaks to (a) III-H1, (b) III-H3, and (c) I-H5.

One of the more interesting results of the simulated annealing was the dramatic increase in the population of the  $\omega = 60^\circ$  state relative to that in the free sugar. For the free sugar, the  $180^\circ$  state of  $\omega$  (B1a) was more represented in the simulated annealing than the  $60^\circ$  state (B2a) by a ratio of

8:5 (Sayers and Prestegard, 2000), but, for the bound sugar, the  $60^\circ$  state was favored by a ratio of 14:1. The question raised is why was the  $60^\circ$  state (MB1 and MB4) so strongly favored? The question is interesting for two reasons: 1) as shown in Table 2, the difference in energy among MB1, MB2, and MB3 is not statistically significant, and 2) modeling easily showed that none of the distances listed in Table

TABLE 1 Results of fitting TrNOESY buildup data to Eq. 1

Proton Pair	$c_2$	$\delta c_2$	$r$ (Å)	$\delta r$
I-H1, I-H2	0.116	0.0160	2.52	—
I-H1, III-H3	0.235*	0.0116	2.25	0.05 <sup>†</sup>
I-H1, III-H4	0.0588*	0.0029	2.82	0.07 <sup>‡</sup>
I-H1, III-H2	0.0150	0.00451	3.54	0.20
II-H1, II-H2	0.162	0.00758	2.51	—
II-H1, III-H6S	0.0801	0.0118	2.82	0.07
II-H1, III-H6R <sup>§</sup>	0.0588	0.0114	2.97	0.10
III-H1, III-H2	0.192	0.00719	2.54	—
III-H1, $\text{OCH}_3$	0.160	0.0302	3.14 <sup>¶</sup>	0.10
III-H2, I-H5	0.132	0.0171	2.70	0.05

\*Corresponds to an 80/20 intensity distribution as described in the text.

<sup>†</sup>Well bottom:  $r_2 = 2.15$ ,  $r_3 = 2.35$ .

<sup>‡</sup>Well bottom:  $r_2 = 2.58$ ,  $r_3 = 3.25$ .

<sup>§</sup>Connectivity contains at least some contributions from indirect pathways.

<sup>¶</sup>Corrected for the degeneracy of the methyl protons.

TABLE 2 Glycosidic dihedral angles in conformations generated in ensemble MB

Conf.*	Energy <sup>†</sup>	I-III $\phi$	I-III $\psi$	II-III $\phi$	II-III $\psi$	II-III $\omega$	$\text{OCH}_3$ $\phi$
MB1	1.260	59.56	-159.30	65.56	-172.25	60.33	64.41
(14)	(0.304)	(5.64)	(11.15)	(1.56)	(0.81)	(1.00)	(0.15)
MB2	1.146	58.46	-160.98	65.03	-175.08	-63.16	64.15
(14)	(0.279)	(1.13)	(1.55)	(0.32)	(0.34)	(0.22)	(0.11)
MB3	0.996	66.89	-144.04	64.30	-172.24	-179.77	63.25
(1)	NA	NA	NA	NA	NA	NA	NA
MB4	1.950	91.11	-63.22	63.55	-173.12	61.60	64.29
(1)	NA	NA	NA	NA	NA	NA	NA

\*Numbers in parentheses indicate the number of structures observed for each conformation.

<sup>†</sup>Mean energy (kJ/mol) of minimized structures, with standard deviations in parentheses.

I are affected by a change in the state of  $\omega$ , indicating that restraints on these distances are powerless in and of themselves to position this torsion. Although the two negatively restrained distances,  $d(\text{II-H1, III-H5})$  and  $d(\text{II-H1, III-H4})$  (one of which was not included in the free trimannoside calculation), are dependent on  $\omega$ , an examination of structures allowed in the presence of these restraints shows that these alone cannot lead to a preference for  $\omega = 60^\circ$ . The most logical explanation is that the differences in restraints on distances across the I–III glycosidic linkage cause changes in the I–III torsion angles that propagate to an  $\omega$  preference through steric interactions. The differences in restraints between solution and bound states are a slight shortening of  $d(\text{I-H1, III-H3})$ , a slight lengthening of  $d(\text{III-H2, I-H5})$ , and the addition of the  $d(\text{I-H1, III-H2})$  restraint. An examination of dynamics trajectories below will show that these result in an average increase in the I–III  $\psi$  angle that correlates with a shift to  $\omega = 60^\circ$ .

### Building a model of the trimannoside complex

Our first task was to build a reasonable starting model for the complex. At this point, the proper orientation of the trimannoside in the MBP-A binding site was unknown. Because the calcium ion in the binding site coordinates both the OH3 and OH4 oxygens, ring I and ring II are both potential ligands because neither could be ruled out on the basis of steric hindrance. Our studies on the free trimannoside provided evidence for subnanosecond internal motions in the molecule, and thus these motions should contribute to line narrowing for noncoordinated residues. After adding MBP-2 at  $5^\circ$ , the linewidths of the three anomeric proton (I-H1, II-H1, and III-H1) resonances in NOESY spectra broadened by 2.8, 1.8, and 0.6 Hz, respectively. The fact that I-H1 displayed the most broadening suggested that ring I is buried deepest within the protein and is thus the ring coordinated to the calcium. Preliminary models for the complex in which either ring I or ring II was coordinated to the calcium revealed that, when ring I is coordinated, the other two rings (II and III) are placed away from protein residues and into solvent, whereas when ring II is coordinated, ring I is thrust into the protein surface, creating highly unfavorable steric clashes. For the latter model to be correct, the bound conformation of the trimannoside would have to be radically different from ones that are consistent with the NMR data, and thus this model was discarded. Interestingly, in the MBP-A/oligosaccharide crystal structure, the oligosaccharide is terminated on one end by a substructure that is equivalent to the trimannoside. In this structure, the ring equivalent to ring I was found to be coordinated to the calcium (Weis et al., 1992). Therefore, all of this evidence suggested that the trimannoside binds to MBP-A in predominantly one orientation, with ring I coordinated to the calcium.

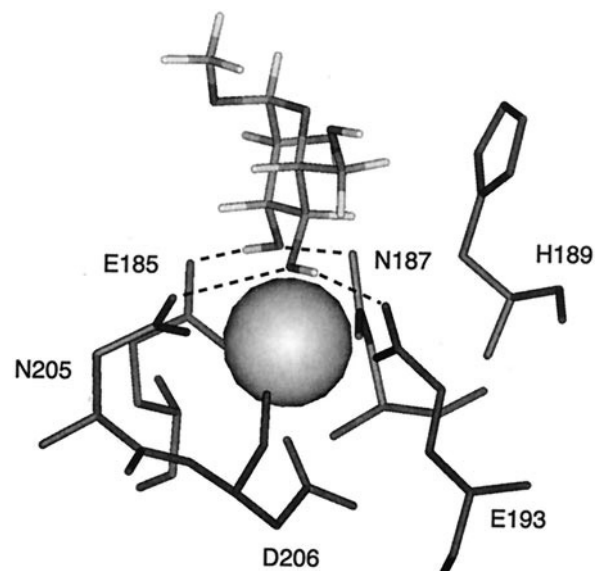


FIGURE 4 Structural model of the MBP-A binding site complexed with  $\alpha$ -Me-Man derived from the crystal structure of Weis et al. (1992). Except for H189, which is involved in a van der Waals contact to the sugar, the labeled residues of MBP-A form the ligands of the binding site calcium, along with the OH3 and OH4 groups of the sugar ligand. The ring atoms of the sugar have been matched to the positions of the terminal mannose residue in the crystal structure. Dashed lines indicate hydrogen bonds between the OH3 and OH4 groups and MBP-A residues.

Given the bound orientation of the trimannoside, AMBER was used to construct models of the MBP-2/trimannoside complex in which the trimannoside assumed conformation MB1, MB2, or MB3. These models will hereafter be referred to as MD(60), MD(-60), and MD(180), respectively, based on the state of II–III  $\omega$ . Because the transitions of  $\omega$  are thought to occur on a microsecond-to-millisecond timescale, they are generally not observed in picosecond-to-nanosecond MD simulations (Brisson and Carver, 1983; McCain and Markley, 1987; Hajduk et al., 1993), and so it was necessary to initialize separate simulations with each of these rotamer states if all of them were to be sampled. Each of these models was minimized and subjected to two rounds of equilibration as described above.

### The calcium coordination shell in the MD simulations

The coordination geometry of the binding site calcium in MBP-2 is a modified pentagonal bipyramid, with planar ligand oxygens provided by E185, N187, E193, N205, and D206; a second D206 oxygen provides one axial position, whereas the other axial position is shared by the O3 and O4 oxygens of the mannose ligand (Weis et al., 1992), resulting in an 8-coordinate calcium (Fig. 4). In addition, the remaining lone pair of O3 accepts a hydrogen bond from N187 H<sup>δ21</sup> whereas the HO3 proton donates a hydrogen bond to

**TABLE 3** RMSD values (Å) for the calcium coordination shell\*

$r^\ddagger$	MD(60)	MD(60)-Ca <sup>‡</sup>	MD(-60)	MD(-60)-Ca <sup>‡</sup>	MD(180)	MD(60t)
Ca <sup>2+</sup> -O3	0.09	0.19	0.09	0.11	0.11	0.10
Ca <sup>2+</sup> -O4	1.17	0.43	2.71	0.44	0.65	0.86
O3-N187	0.46	0.41	1.47	0.43	0.43	0.41
HO3-E185	1.16	1.54	2.53	0.31	1.17	0.35
O4-N205	0.86	1.23	1.81	0.84	0.76	0.74
HO4-E193	0.22	0.26	0.66	0.26	0.22	0.24
Overall	1.93	2.08	4.43	1.13	1.61	1.28

\*RMSD values were calculated relative to the bond lengths in the crystal structure of Weis *et al.* (1992).

<sup>‡</sup>O3, O4, HO3, and HO4 represent the oxygens and protons of the indicated hydroxyl groups of ring I. N187 and N205 represent their H<sup>δ21</sup> protons, and E185 and E193 represent their O<sup>ε2</sup> atoms.

<sup>‡</sup>These runs included restraints on the Ca<sup>2+</sup>-O3 and Ca<sup>2+</sup>-O4 bonds.

E185 O<sup>ε2</sup>; an equivalent relationship exists between (O4, N205) and (HO4, E193), for a total of four hydrogen bonds and two coordination bonds (Weis *et al.*, 1992; Sayers *et al.*, 1998). These six interactions are thought to be the primary stabilizing forces of this binding site, and thus the integrity of these bonds was analyzed first.

Initially, the calcium and the bound trimannoside were allowed to evolve under the influence of the AMBER force field alone without explicit bonds or restraints between them. The calcium was also not restrained in its interaction with protein ligands. In general, the protein ligands of the calcium maintained their positions throughout all of the simulations, leaving that portion of the coordination shell fully intact; however, from the root-mean-square deviation (RMSD) values listed in Table 3, it is clear that, in MD(-60), the bonds involving the trimannoside in the coordination shell showed particularly poor behavior. The trajectories indicated that the shell disrupted within 20 ps, leaving only bonds Ca<sup>2+</sup>-O3 and E193 O<sup>ε2</sup>-HO4 at their canonical values. The trajectories of MD(60) and MD(180) revealed much smaller distortions resulting from brief (10–20 ps), transient tilting of the trimannoside toward the MBP-2 surface by ~10–15°. In MD(-60) and MD(60) simulations in which the Ca<sup>2+</sup>-O3 and Ca<sup>2+</sup>-O4 bonds were restrained to the values in the crystal structure, the behavior of MD(-60) improved; however, for MD(60) the precise nature of the distortions differed when these restraints were included, but the results were qualitatively the same.

### The α(1→3) linkage retains flexibility in the bound state

A close examination of the MD trajectories for I–III  $\phi$  and  $\psi$  demonstrated that  $\psi$  was often dynamic in these simulations. Example ( $\phi$ ,  $\psi$ ) trajectories from an MD(60) simulation are shown in Fig. 5, along with RMSDs to the TrNOESY data computed for the restrained distances of the I–III linkage. The RMSD data clearly show that, when the TrNOE for d(I–H1, III–H4) was satisfied, the TrNOEs for

d(I–H1, III–H3) and d(H1, III–H2) were not, and vice versa, strongly suggesting that a single ( $\phi$ ,  $\psi$ ) conformation cannot satisfy the data. Interestingly, the change in RMSD values is strongly correlated with the value of  $\psi$ , suggesting that models with multiple  $\psi$  states may satisfy the TrNOESY data. Given the short duration of the MD simulations, it is unlikely that transitions in  $\psi$  were sampled adequately, and therefore data such as that in Fig. 5 cannot be used to predict relative populations of the  $\psi$  states. However, straightforward calculations were able to show that the TrNOESY data could be satisfied by models in which ( $\phi$ ,  $\psi$ ) states near (85°, -105°) and (75°, 195°) were populated in a ratio of ~3:1. This behavior is remarkably similar to that observed for the free sugar, where ( $\phi$ ,  $\psi$ ) for this linkage was found to populate two states, (80°, -100°) and (60°, -180°) in a ratio of ~1.5:1 (Sayers and Prestegard, 2000). The data therefore indicate that the flexibility of the I–III linkage found in the free sugar is maintained upon binding to MBP-2.

### The ω = 60° state of the α(1→6) linkage is preferred in the binding site

The results of the unrestrained MD simulations are further summarized in Table 4, in which are listed the mean values of the six glycosidic dihedral angles for MD(60), MD(180), and MD(-60), along with another model labeled MD(60t). MD(60t) resulted from a transition of  $\omega$  observed in MD(180) simulations. In two of the three MD(180) simulations performed,  $\omega$  surprisingly shifted from 180° to 60° in less than 40 ps, converting model MD(180) into MD(60). In both cases,  $\omega$  then maintained the 60° state for the remainder of the simulations. To simplify subsequent analyses, the MD(180) trajectories were divided into two data sets based on the state of  $\omega$ , and these sets are labeled MD(180) and MD(60t). From Table 4 it is apparent that, apart from the obvious differences in  $\omega$ , the α(1→6)  $\phi$  and  $\psi$  torsions in MD(60), MD(60t), and MD(180) behaved similarly; indeed, the only significant ( $\phi$ ,  $\psi$ ) transition in the trajectories was one of  $\psi$  from 180° to 60° in MD(60) (reflected in the larger standard deviation), very similar to

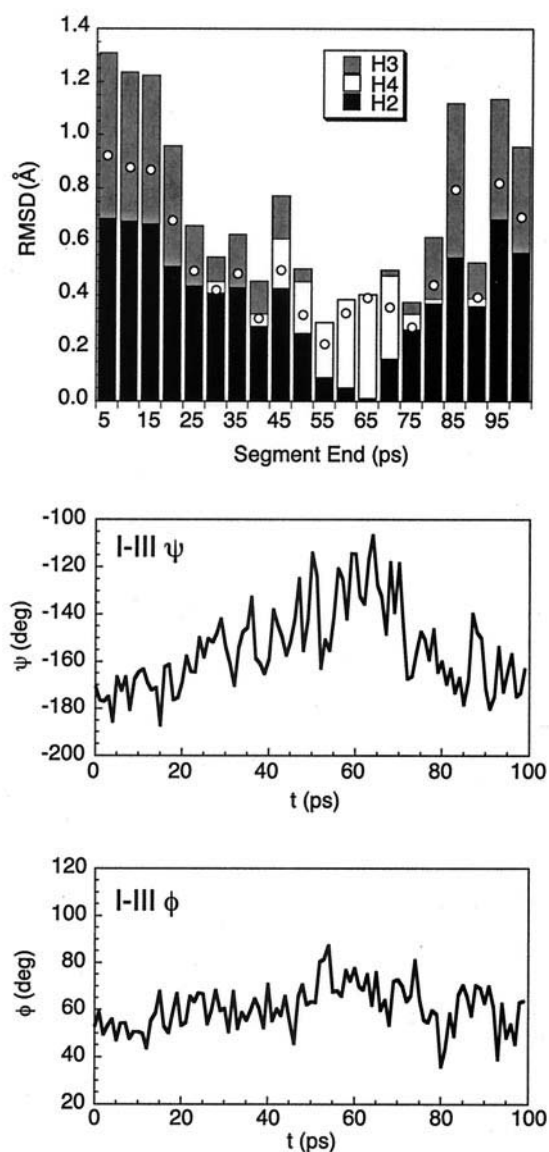


FIGURE 5 Data showing the effects of the dynamics of the I-III linkage on RMSD values. RMSD values for each distance were calculated from the well limit ( $r_2$  or  $r_3$ ) closer to the MD average value (Table 5). If the MD average lay between  $r_2$  and  $r_3$ , the RMSD was set to zero. The top graph shows RMSD values for three distances from I-H1 to the labeled protons on ring III (i.e., H3 = d(I-H1, III-H3)). These values were calculated for 5-ps segments of a 100-ps MD(60) simulation. Overall RMSD values for these three distances are indicated by circles. All of these data are plotted according to the end of each 5-ps segment. The two lower graphs show the corresponding trajectories of I-III  $\psi$  and  $\phi$ , respectively.

behavior observed for the free sugar. In contrast, the behavior of the torsions of both linkages in MD(-60) was unique. The behavior of the  $\alpha(1\rightarrow6)$  linkage in MD(-60) was especially complex, populating highly unusual states of  $\phi$  ( $180^\circ$ ) and shifting  $\omega$  from  $-60^\circ$  to  $60^\circ$ . Although this shift in  $\omega$  would seem to have converted model MD(-60) into MD(60), this was not the case because of the unusual state of  $\phi$  ( $180^\circ$ ). This change was correlated with disruption of

TABLE 4 Mean dihedral angles from MD trajectories

Model*	I-III $\phi$	I-III $\psi$	II-III $\phi$	II-III $\psi$	II-III $\omega$	OCH <sub>3</sub> $\phi$
MD(60)	59.77 <sup>†</sup>	-155.18	63.74	163.10	59.97	68.41
(330)	(9.70)	(16.75)	(13.20)	(39.07)	(10.72)	(18.06)
MD(60t)	57.60	-151.14	65.74	178.19	63.32	71.29
(118)	(10.71)	(21.63)	(14.45)	(15.36)	(14.34)	(22.40)
MD(180)	57.60	-164.85	63.67	169.01	179.62	63.84
(102)	(8.90)	(15.68)	(10.80)	(14.45)	(13.38)	(11.57)
MD(-60)	68.45	116.13	135.51	183.62	-119.16	70.52
(100)	(18.23)	(31.63)	(35.61)	(16.34)	(47.66)	(16.68)
	60	-180				
Free	80	-100	65	180 (60)	60/180	68 (150)

\*Values in parentheses indicate the total length of the combined trajectories in picoseconds.

<sup>†</sup>Mean values in degrees. Values in parentheses are standard deviations.

the calcium coordination shell and probably indicates some inherent instability in complexes with this ligand geometry.

Given that the  $\omega = 60^\circ$  state appeared to be favored in the MD simulations, the question arises as to whether there was a structural basis for this preference. In Fig. 6 are shown representative structures from the MD trajectories of the four models. These structures depict several additional hydrogen bonds between the trimannoside and MBP-2 in addition to those of the calcium coordination shell. These hydrogen bonds were generally transient, lasting a few tens of picoseconds. Concentrating first on the MD(60), MD(180), and MD(-60) structures (Fig. 6, A, C, and D), it is clear that the principal difference between these structures arises from the position of ring II, which is largely determined by  $\omega$ . The bent nature of the  $\omega = 60^\circ$  state, which directs ring II toward the MBP-2 surface, allows a direct hydrogen bond to form between II-O3 and an H $^\epsilon$  of K182. In contrast, the other two  $\omega$  states direct ring II away from MBP-2 and out into solvent, preventing any contacts between this ring and K182. Instead, in MD(180) K182 contacts III-O<sub>2</sub> and a water molecule (HOH3) that mediates further interactions with III-O5 and III-O6; however, in MD(-60), III-O6 was turned further outward relative to its position in MD(60) and MD(180), and all contacts between this atom and MBP-2 were lost. Remarkably, in both cases, after the shift in  $\omega$  from  $180^\circ$  to  $60^\circ$  in MD(180) simulations, the K182 side chain subsequently closed the distance between itself and ring II, forming, in the case shown in Fig. 6 B, the same direct hydrogen bond to ring II as in MD(60). As shown in Fig. 7, after the  $\omega$  transition, the distances between II-O3 and the terminal amino protons of K182 decreased from near 10 Å to near 2 Å as I-III  $\psi$  shifted from  $-180^\circ$  to  $-130^\circ$ . This same  $\psi$  transition was separately observed (Fig. 5) and is supported by the TrNOESY data. The only apparent consequence of the difference in ( $\phi$ ,  $\psi$ ) states in Fig. 6 A ( $72.7^\circ$ ,  $-162.2^\circ$ ) and 6 B ( $65.0^\circ$ ,  $-130.8^\circ$ ) is a slight rearrangement of associated solvent. Therefore, in general, it seems that the  $\omega = 60^\circ$  structures enable all three rings of the trimannoside to make direct or water-mediated

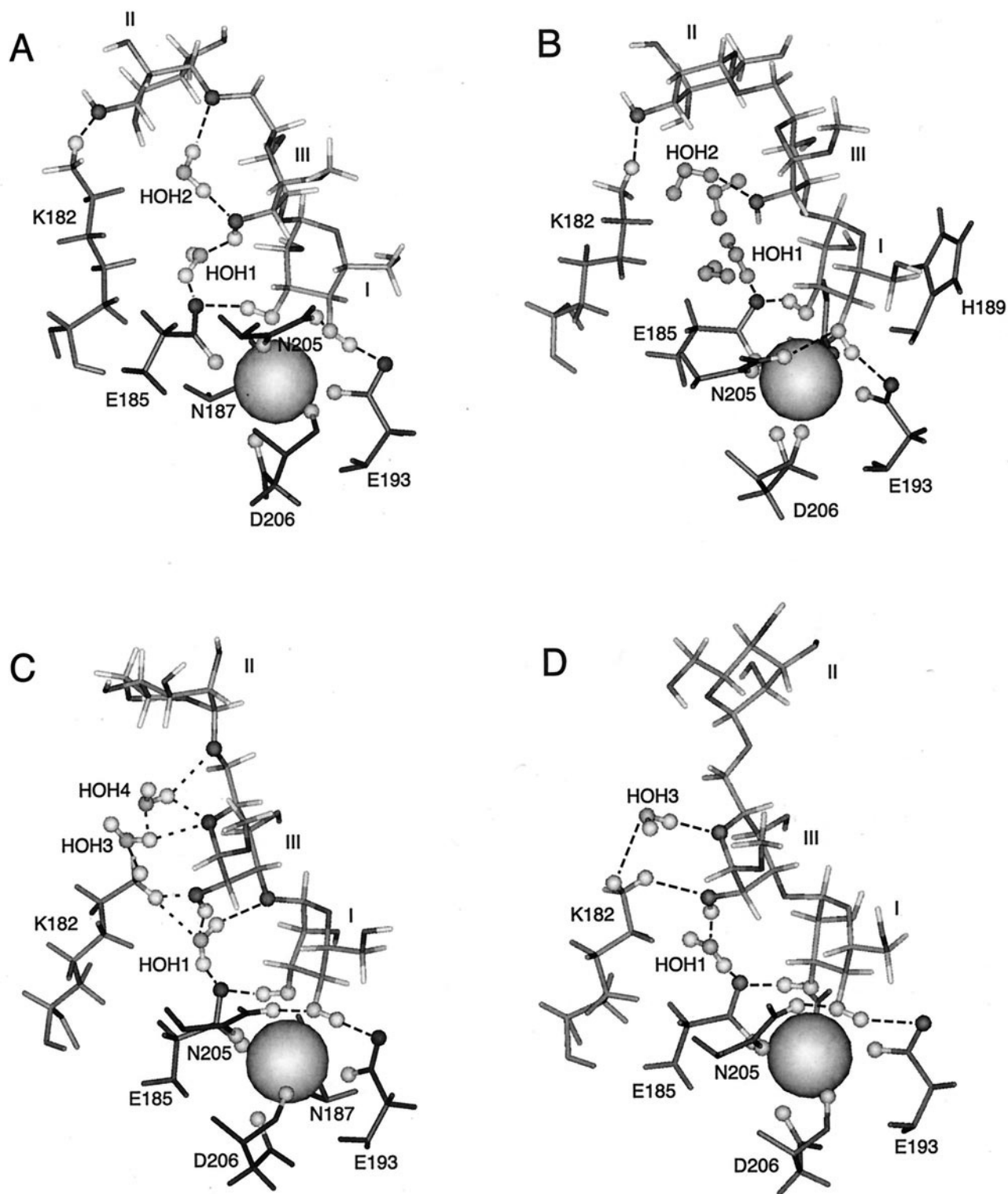


FIGURE 6 Structures of the MBP-2 binding site complexed with the trimannoside derived from MD simulations: (A) MD(60), (B) MD(60t), (C) MD(180), (D) MD(-60). Atoms represented as small spheres are either calcium ligands or are involved in hydrogen bonds. Hydrogen bonds are represented by heavy dashed lines. Light dashed lines (i.e., involving HOH4 in (C)) indicate situations where more than one hydrogen bond is possible for the donor.

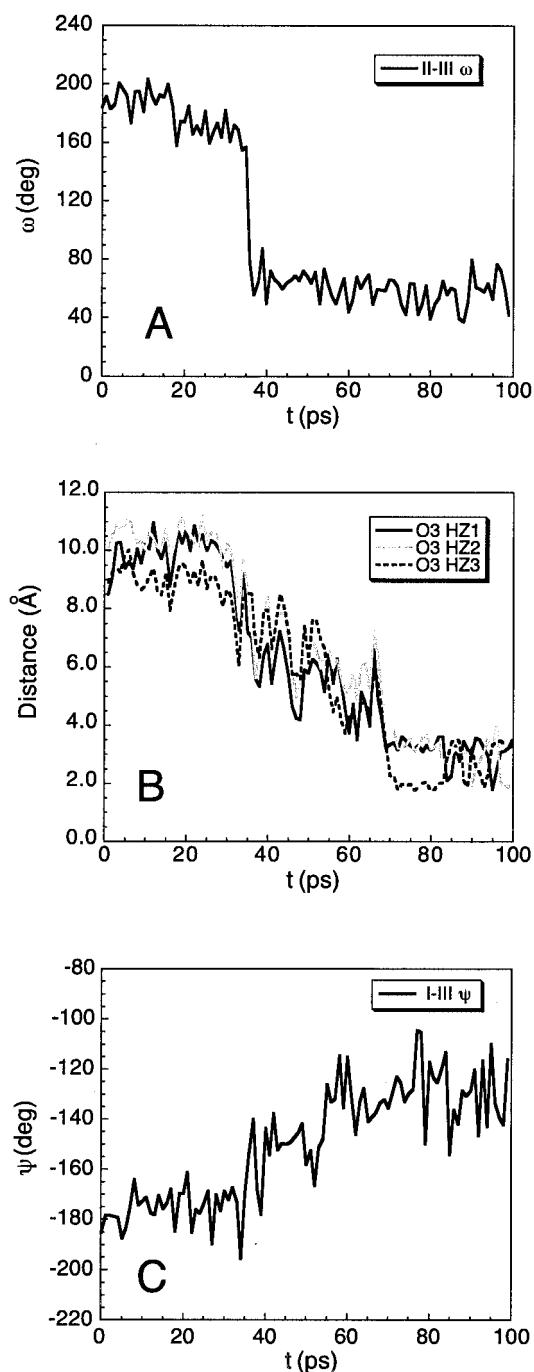


FIGURE 7 MD trajectories from an MD(180) simulation showing the formation of the (K182-H $\epsilon^i$ , II-O3) hydrogen bond after a II-III  $\omega$  transition. (A) Trajectory of I-II  $\omega$  showing the 180° $\rightarrow$ 60° transition. (B) Trajectories of  $d(\text{K182-H}\epsilon^i, \text{II-O3})$  for the three K182 H $\epsilon^i$  protons. (C) Trajectory of I-III  $\psi$ .

contacts with MBP-2 residues. These interactions may contribute to the selection of the  $\omega = 60^\circ$  state in the bound form of the trimannoside.

In addition to interactions with K182, the role of water molecules also appears to be important in these complexes.

In spite of the differences among the models, there is a striking similarity in all three structures: a water labeled HOH1 is placed so that it can form a bridge between III-HO2 and the available lone pair of E185 O $\epsilon^2$ . In MD(60), the space between the K182 side chain and the trimannoside was filled by HOH1 and another water, HOH2. The bridge mediated by HOH1 was quite stable in these simulations, in one case lasting for an entire run of 80 ps. In MD(60) HOH2 bridged III-O $_2$  and III-O $_6$ , and was close to being within hydrogen bonding distance of another K182 H $\epsilon^i$ . Interestingly, although HOH1 mediated the same bridge in MD(180) and MD(-60) as it did in MD(60), the interactions mediated by other waters were more variable, suggesting a lower stability for these models than for the well-ordered state of MD(60).

Finally, when considering the structures in Fig. 6, it is important to note that these are not static structures, but are subject to considerable adjustment of trimannoside torsion angles and protein side-chain conformations and associated solvent interactions. Although these dynamics may allow interconversions among the models shown, they may also allow additional interactions. For example, in an MD(60) simulation, the trimannoside tilted briefly toward MBP-2 as a result of lengthening of the Ca $^{2+}$ -O4 bond. Although this distorted the calcium coordination shell, it allowed a second hydrogen bond to form between II-HO4 and the O $\delta^2$  of D184, a side chain that approached ring II from the opposite side relative to K182. Such additional bonds might partly compensate for those weakened in the calcium shell. The maintenance of these levels of flexibility and variation in hydrogen bonding patterns may significantly compensate for unfavorable entropy losses on ligand binding.

### Comparison of MD models and MR data

To evaluate the models for the complex seen in the MD simulations in light of the NMR data,  $\langle r^{-6} \rangle^{-1/6}$  averages were calculated for the experimentally restrained distances from the MD trajectories for each model. A comparison of these averages to experimental restraints from NOESY data is strictly valid only where the transitions among states are slow compared to molecular tumbling. However, the approximation is widely used and adequate for our purposes. The derived distances, along with distances for selected static structures from simulated annealing ensemble MB, are collected in Table 5. RMSD values for these averages were also computed relative to the experimental ranges determined from the TrNOESY data, and these are depicted in Fig. 8. From Table 5, it is clear that neither the average distances back-calculated from MD(60), MD(60t), nor MD(180) fit the experimental data very well. Some of the discrepancy may come from indirect magnetization transfers, in  $d(\text{II-H1}, \text{III-H6S})$  and  $d(\text{II-H1}, \text{III-H6R})$  for example, where the H6S-H6R distance is very short. The TrNOE value for III-H6S (2.82 Å) was generally larger than the MD

**TABLE 5** Values of restrained internuclear distances (Å) in selected models

Distance	Experiment*	$\omega = 60^\circ$			$\omega = 180^\circ$		$\omega = -60^\circ$	
		Static	MD(60) <sup>†</sup>	MD(60t) <sup>†</sup>	Static	MD(180) <sup>†</sup>	Static	MD(-60) <sup>†</sup>
I-H1, III-H3	2.15–2.35	2.86	2.72	2.65	2.60	2.87	3.00	3.59
I-H1, III-H4	2.58–3.25	3.35	3.36	3.31	3.66	3.14	3.22	2.40
I-H1, III-H4	3.34–3.74	4.50	4.34	4.30	4.35	4.46	4.56	3.83
III-H2, I-H5	2.65–2.75	2.72	2.52	2.47	2.53	2.71	2.81	4.45
II-H1, III-H6R	2.87–3.07	2.87	3.01	2.90	2.93	3.05	2.95	2.36
II-H1, III-H6S	2.75–2.89	2.50	2.45	2.41	2.52	2.32	2.49	2.52
II-H1, III-H5	>4.00	4.72	4.42	4.62	4.30	3.93	4.55	4.20
II-H1, III-H4	>4.00	4.59	3.83	4.52	5.24	5.11	4.37	4.18
III-H1, OCH <sub>3</sub>	3.04–3.24	2.89	2.84	2.83	2.90	2.87	2.90	2.82

\*Distance ranges in Å consistent with TrNOESY data.

<sup>†</sup> $\langle r^{-6} \rangle^{-1/6}$  in Å calculated over the indicated MD trajectories.

distances, whereas, for III-H6R, the TrNOE value (2.97 Å) was smaller than the MD distances. This is consistent with magnetization transferring from III-H6S to III-H6R causing the TrNOESY data to overestimate d(II-H1, III-H6S) and underestimate d(II-H1, III-H6R). Similar arguments do not, however, explain the discrepancies for d(I-H1, III-H3) and d(I-H1, III-H2); however, as described above, these restraints can be satisfied by two states of I–III  $\phi$  and  $\psi$ . Because the timescale of the  $\psi$  transitions ( $\sim 100$  ps) is on the same order as the lengths of the simulations, it is likely that these transitions were incompletely sampled, rendering the MD averages only approximations of the true average values observed in the NMR experiment. Nevertheless, from Fig. 8, it would appear that the  $60^\circ$  state allowed the

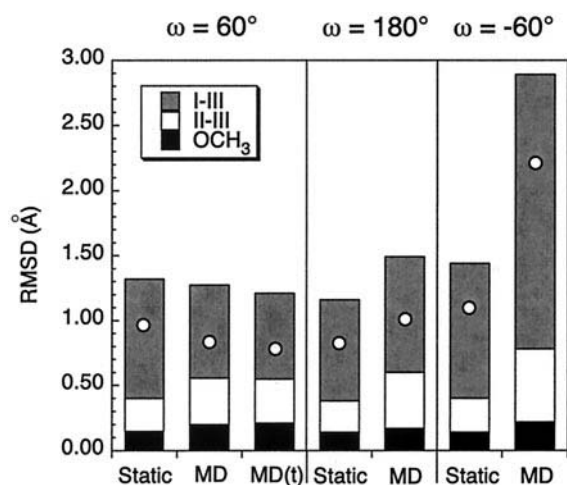


**FIGURE 8** RMSD values for models of the MBP-2/trimannoside complex calculated from the data in Table 5. The models are grouped according to the state of II–III  $\omega$ , shown above the plot, and represent both static models and models taken from MD trajectories. RMSD values were calculated as described in the legend to Fig. 5. Combined RMSD values of the restrained distances of the I–III, II–III, and OCH<sub>3</sub> linkages are displayed as gray, white, and black bars, respectively. The overall RMSD values for all restrained distances are indicated by circles. For  $\omega = 60^\circ$ , MD(60) and MD(60t) data are labeled as MD and MD(t), respectively.

best overall fit to the TrNOESY restraints. Notably, the  $60^\circ$  state is the only state for which the averaging provided by the MD simulations decreased the overall RMSD (and that for the I–III linkage) relative to that of the static structures. Also, in the MD(60t) simulations, the overall RMSD decreased 0.23 Å on average as a result of the  $\omega$  transition.

The question still remains as to why the  $\omega = 60^\circ$  state reduced the RMSD to the NMR data when few of the data directly restrain  $\omega$ . One possibility is that the state of the I–III linkage affects the behavior of  $\omega$ . Indeed, such a correlation was suggested by our studies of the free trimannoside. Histograms of I–III  $\psi$  values derived from the trajectory of MD(180) and the combined trajectories of MD(60) and MD(60t) are displayed in Fig. 9. As shown, the distribution of  $\psi$  for  $\omega = 60^\circ$  is shifted toward higher values relative to that for  $\omega = 180^\circ$  (an increase of  $10.4^\circ$  in the mean). As described above, the NMR data are consistent with a model in which  $\psi$  samples states near  $-105^\circ$  and  $-195^\circ$ , with the former state being dominant. Again, because the timescale of the transition between these states is similar to the simulation lengths, these histograms largely reflect the transitions themselves rather than reliable populations. Nevertheless, the shift to higher values of  $\psi$  when  $\omega = 60^\circ$ , which would need to be verified by longer simulations, is perhaps a means by which the  $\omega = 60^\circ$  state achieves a closer fit to the NMR data.

### Calculations of accessible surface areas also favor the $\omega = 60^\circ$ state

Further insight into the complexes shown in Fig. 6 was provided by computing the changes in water-accessible surface area ( $-\Delta$ ASA) upon binding. The results of such calculations are displayed in Table 6, in which the total  $-\Delta$ ASA values have been separated into the contributions from various structural groups. Interestingly, these calculations revealed several additional MBP-2 residues that showed substantial  $-\Delta$ ASA values upon trimannoside binding (generally  $10\text{--}30 \text{ \AA}^2$ ). These residues, S154, H189,

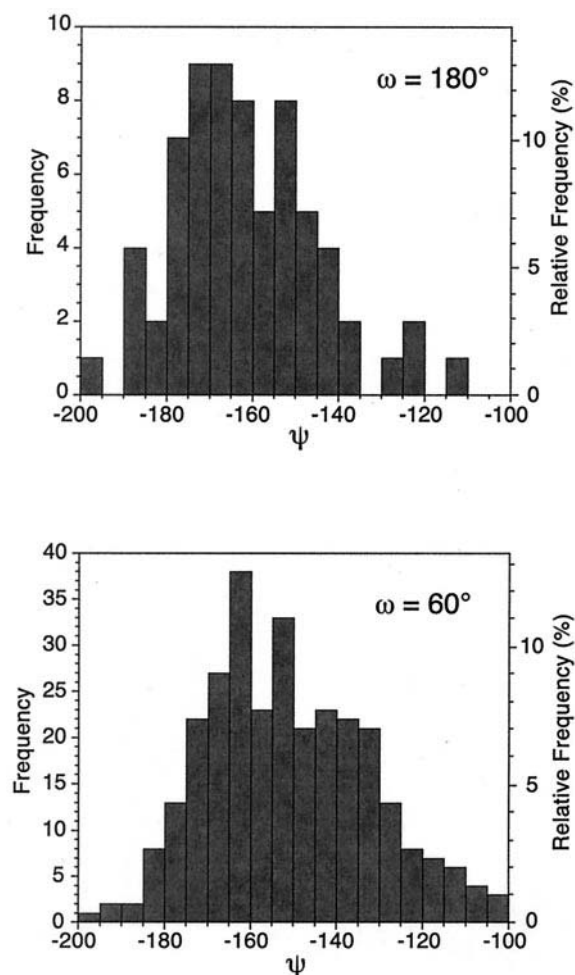


FIGURE 9 Histograms of the I-III  $\psi$  dihedral angle derived from MD trajectories. Data for  $\omega = 180^\circ$  were taken from MD(180) trajectories, whereas data for  $\omega = 60^\circ$  were taken from combined MD(60) and MD(60t) trajectories.

V199, and I207, appear to be involved in van der Waals contacts between MBP-2 and the trimannoside, and are collected together as VDW Set in Table 6. S154, V199, and I207 lie above E185, N205, and D206 on the opposite side of the trimannoside from H189 as depicted in Fig. 6 B (if shown, they would obscure the trimannoside and hydrogen-bonding network). A methyl group of I207 generally lies 2.5–3.0 Å from the exocyclic methylene protons of ring I, while methylene and methyl groups of S145 and V199 lie within 2.5–4.0 Å of the OCH<sub>3</sub> attached to ring III. As shown in Fig. 6 B, the side chain of H189 is stacked against ring I as described in the crystal structure (Weis et al., 1992). However, in the MD(60) structure, the H189 side chain was tilted further away from ring I, and is not shown in Fig. 6 A. The data in Table 6 clearly show that the MD(60) complex buries ~60–100 Å<sup>2</sup> more surface area than the other models, and that the majority of this difference occurs at rings II and III. Notably, the  $-\Delta\text{ASA}$  for ring

TABLE 6 Changes in water-accessible surface area ( $-\Delta\text{ASA}$ ) upon binding (Å<sup>2</sup>) and derived thermodynamic estimates at 298 K (kJ/mol)

Residues	MD(60)	MD(60t)	MD(-60)	MD(180)	$\alpha$ -Me-Man
Ring I	144.4	158.7	128.5	148.5	170.5
Ring II	42.2	35.0	0.0	0.0	—
Ring III + OCH <sub>3</sub>	93.2	9.3	61.9	65.1	—
Calcium Shell*	61.9	56.3	80.4	71.0	37.5
K182	50.9	54.2	46.5	34.3	0.0
VDW Set <sup>†</sup>	52.5	46.5	32.8	63.8	39.4
Other <sup>‡</sup>	1.9	2.7	0.2	0.4	0.0
<b>Total</b>	<b>447.0</b>	<b>362.7</b>	<b>350.3</b>	<b>383.1</b>	<b>247.4</b>
$\Delta\text{ASA}_{\text{pol}}$	251.4	265.5	235.9	254.1	158.4
$\Delta\text{ASA}_{\text{ap}}$	195.6	97.2	114.4	129.0	89.0
$\Delta H$	-43.5	-48.8	-42.7	-46.0	-28.4
$T\Delta S_{\text{solv}}^{\S}$	10.3	-2.1	1.5	2.2	2.4
$T\Delta S_{\text{t-or}}^{\parallel}$	-10.9	-10.9	-10.9	-10.9	-10.9
$T\Delta S_{\text{rot}}$	-25.3	-16.6	-19.5	-26.3	-3.8
$\Delta G$	-17.6	-19.2	-13.8	-11.0	-16.1
$K_a$ (M <sup>-1</sup> ) est.	1200	2300	260	85	660

\*E185, N187, E193, N205, D206, Ca<sup>2+</sup> (binding site).

<sup>†</sup>S154, H189, V199, I207.

<sup>‡</sup>MD(60): D200, H213; MD(60t): K183, D184; MD(-60): H213; MD(180): S208.

<sup>§</sup>Corresponds to  $T\Delta S_{\text{solvlc}}$  in (García-Hernández and Hernández-Arana, 1999).

<sup>||</sup>Corresponds to  $T\Delta S_{\text{t-orlc}}$  in (García-Hernández and Hernández-Arana, 1999).

II is zero in models MD(-60) and MD(180), confirming the total lack of interactions between this ring and MBP-2 in these complexes. Interestingly, the  $-\Delta\text{ASA}$  value for ring III and the OCH<sub>3</sub> group is dramatically reduced in MD(60t) compared to MD(60), and this change is almost totally responsible for the difference in total  $-\Delta\text{ASA}$  between these models. This seems to be correlated with the rearrangement of the ordered waters in MD(60t) discussed above, allowing more mobile waters to lie between ring III and the K182 side chain.

Recently, a method was proposed by which binding constants for carbohydrate-protein complexes could be estimated in part from changes in polar ( $\Delta\text{ASA}_{\text{pol}}$ ) and apolar ( $\Delta\text{ASA}_{\text{ap}}$ ) surface areas to within one order of magnitude (García-Hernández and Hernández-Arana, 1999). The resulting thermodynamic parameters, also listed in Table 6, were calculated as described by these authors, except that the entropy cost of freezing bond rotations ( $T\Delta S_{\text{rot}}$ ) also included contributions to account for water molecules involved in hydrogen bonds. The entropy loss for transferring a water molecule from bulk solvent to a protein site has been placed between 0 and 29 J/K-mol (Dunitz, 1994), and has been measured to be 10.4 J/K-mol in ribonuclease A (Mrevlishvili, 1998). The latter value compares well to that found for the average entropy loss from freezing the rotation of two bonds of an amino acid side chain (12.8 J/K-mol) (Doig and Sternberg, 1995; García-Hernández and Hernán-

**TABLE 7** Bound conformations determined for the trimannoside in lectin binding sites

	I–III $\phi$	I–III $\psi$	II–III $\phi$	II–III $\psi$	II–III $\omega$	Reference
Free solution	60 80	–180 –100	64	180 (60)	60 (180)	(Sayers and Prestegard, 2000)
MBP-2	75 85	–195 –105	64	180	60	This work
MBP-A CRD*	76	–99	ND <sup>†</sup>	–146	47	(Weis et al., 1992)
Concanavalin A <sup>‡</sup>	90 ± 30	–121 ± 9	65 ± 11	–174 ± 3	70 ± 10	(Loris et al., 1996)
Concanavalin A <sup>‡</sup>	66 ± 2	–115 ± 5	66 ± 2	–170 ± 3	75 ± 4	(Naismith and Field, 1996)
<i>D. grandiflora</i> lectin <sup>‡</sup>	68 ± 7	–111 ± 3	63 ± 2	–168 ± 5	79 ± 5	(Rozwarski et al., 1998)
<i>G. nivalis</i> agglutinin CRD 1	87	–65	74/77	–177/–158	180/44	(Wright and Hester, 1996)
CRD 2	ND	ND	75	107	172	
CRD 3	69	–121	81	102	177	

\*The crystallized MBP-A CRD differs from MBP-2 in that it consists of residues 107–221 of MBP-A, whereas MBP-2 consists of residues 109–221.

<sup>†</sup>ND, not determined.

<sup>‡</sup>Values are averages and standard deviations of the four binding sites of the lectin tetramer.

dez-Arana, 1999), and so the loss per water molecule was estimated to be 10 J/K-mol (or 5 J/K-mol for a water with only one hydrogen bond). To evaluate each model separately, contributions for freezing II–III  $\psi$  and  $\omega$  were included in  $\Delta S_{\text{rot}}$ ; however, contributions for the other glycosidic torsions were not included because our data indicate that their dynamics does not change upon binding. For comparison, data for the complex of MBP-2 with  $\alpha$ -Me-Man are also included. Clearly, the resulting estimates of binding constants also suggest that the  $\omega = 60^\circ$  state is the dominant bound conformation. The somewhat higher binding constant estimated for MD(60t) is also consistent with the NMR data, which suggest that the  $\psi \sim -120^\circ$  state found in this structure should dominate. However, it is notable that, if the H189 side chain were tilted away from ring I in the MD(60t) structure so that it has no effect on the ASA values (as is the case for MD(60)), the smaller  $-\Delta\text{ASA}$  values would reduce  $K_a$  by a factor of 4 for this model ( $K_a \rightarrow 520 \text{ M}^{-1}$ ). This result is remarkably similar to that of mutation studies where H189 was replaced by a glycine, reducing  $K_a$  by a factor of 5 (Iobst et al., 1994). Finally, these estimates based on ASA values compare favorably with prior experimental measurements of  $K_a$  for  $\alpha$ -Me-Man ( $340 \text{ M}^{-1}$  [Iobst et al., 1994],  $1000 \text{ M}^{-1}$  [Quesenberry et al., 1997], and  $1700 \text{ M}^{-1}$  [Lee and Lee, 1997; Lee et al., 1999]) and an  $\text{IC}_{50}$  value of 0.94 mM for the trimannoside (Lee and Lee, 1997).

## DISCUSSION

### Description of the structural model

The results of our previous study of the free trimannoside indicated a very dynamic molecule having at least four major states interconnected by transitions at the I–III and II–III linkages. The transitions of the II–III  $\omega$  dihedral angle played the largest role in changing the overall shape of the molecule. A state with  $\omega = 180^\circ$  resulted in a linear mol-

ecule, whereas a state with  $\omega = 60^\circ$  resulted in a molecule bent by  $\sim 80^\circ$  at the II–III linkage. The  $\omega = -60^\circ$  state is known to be vanishingly populated in solution (De Bruyn and Anteunis, 1976), and this was confirmed based on measurements of three-bond coupling constants. Although such coupling constants for the bound state are not accessible in the types of experiment presented here, the combination of TrNOESY data and MD data presented also exclude a  $\omega = -60^\circ$  state for the bound conformation. However, other significant differences between free and bound states arise. Although the population ratio of the two  $\omega$  states in the free sugar was found to be  $\sim 2:1$  in favor of  $\omega = 60^\circ$ , our TrNOESY and MD data suggest that this ratio shifts significantly more toward the  $60^\circ$  state in the MBP-2 complex. Moreover, the thermodynamic estimates for the bound state in Table 6 favor the  $60^\circ$  over the  $180^\circ$  state.

Our results also indicate that the dynamics of the  $\alpha(1\rightarrow3)$  linkage in the free trimannoside are largely maintained in the MBP-2 binding site. These dynamics arise largely from transitions of  $\psi$  between a major state of  $-110 \pm 10^\circ$  ( $P \sim 0.75$ ) and a minor state of  $-180 \pm 10^\circ$  ( $P \sim 0.25$ ). These dynamics are supported by our TrNOESY and MD data, and modeling suggests that these motions may be functionally important in compensating for potential entropy losses on forming the (K182-H $^\zeta$ , II-O3) hydrogen bond. Indeed, by populating both states of I–III  $\psi$ , the (K182-H $^\zeta$ , II-O3) hydrogen bond could be maintained during changes in the conformation and position of the K182 side chain. Moreover, the MD simulations suggest that these dynamics also partially disrupt the ordered waters between the trimannoside and K182, further reducing the entropic cost.

### Comparison to related structures

The bound conformation derived from our data agrees well with that determined from several crystal structures of lectin/trimannoside complexes, as summarized in Table 7. As

mentioned previously, one terminus of the oligosaccharide complexed to the MBP-A CRD (Weis et al., 1992) corresponds exactly to the trimannoside used in our study. Even though the ring corresponding to ring II was not visible in the electron-density map, sufficient density was present to define  $\omega$  to be in the  $60^\circ$  state, as in our model. Also, I–III  $\psi$  was found to be in the major conformation of our model ( $-110^\circ$ ). The invisibility of ring II is perhaps consistent with our simulations showing that motion of the side chain of K182 in concert with trimannoside motions allow maintenance of the (K182 H<sup>ε</sup>, II-O3) hydrogen bond. In addition, our model supports the binding site orientation of the terminal mannose residue as determined in the MBP-A/oligosaccharide crystal structure. Notably, if ring I is rotated  $180^\circ$  in the binding site so that it adopts the bound geometry observed for MBP-C, rings II and III are directed out into solvent regardless of the  $\omega$  state, and no interactions between these rings and MBP-A are possible.

Regarding other structures, both concanavalin A complexes and that of the closely related *Digitalis grandiflora* lectin placed the trimannoside in essentially the same conformation as in our model, while the *Galanthus nivalis* agglutinin structure placed trimannoside molecules in both the  $\omega = 60^\circ$  and  $\omega = 180^\circ$  states, with two CRDs placing II–III  $\psi$  close to the  $60^\circ$  value transiently observed in MD(60). Moreover, our model agrees quite well with a recent statistical analysis of available oligosaccharide crystal structures (Petrescu et al., 1999). In these structures, the two most populated  $\omega$  states ( $66.4 \pm 10.2^\circ$  and  $185.0 \pm 11.2^\circ$ ) are equivalent to the  $60^\circ$  and  $180^\circ$   $\omega$  states of our model, and, likewise, the  $\alpha(1\rightarrow3)$  ( $\phi, \psi$ ) state ( $72.5 \pm 11.0^\circ, -112.3 \pm 22.5^\circ$ ) is also equivalent to the major ( $\phi, \psi$ ) state in our model. Therefore, it appears that, in the structures determined to date, lectins tend to bind a subset of conformations that the trimannoside samples in solution, favoring properties represented by the structures shown in Fig. 6, A and B.

The energetic bases for the selection of these bound conformations are also consistent with previous suggestions. Hydrogen bonds made both directly with protein side chains and mediated by water molecules, in addition to van der Waals contacts, play important roles in these interactions. In the electron density map of the MBP-A/oligosaccharide complex, the K182 side chain of one CRD formed a direct hydrogen bond to the OH4 of the penultimate mannose residue of the ligand (Weis et al., 1992). In related CRDs, similar direct hydrogen bonds involving positively charged side chains have been observed. In the crystal structure of the K3 mutant of MBP-A, K211 formed a direct hydrogen bond to the ligand, a Lewis<sup>x</sup> oligosaccharide. Also, in the closely related CRD from rat hepatic lectin I (specific for galactose), R236 and G238, in positions corresponding to those of K182 and D184 of MBP-A, appeared to enhance the selectivity of this lectin for N-acetylgalactosamine over galactose, most likely through a hydrogen

bond between R236 and the acetyl group of the sugar (Iobst and Drickamer, 1996). Considering van der Waals contacts, the MBP-A CRD crystal structure revealed two primary contacts to H189 and I207, both of which are members of our van der Waals set. Finally, considering the role of water molecules, our structures demonstrate the typical water-mediated hydrogen bonds long observed in protein–carbohydrate complexes (Quioco, 1989; Toone, 1994). Notably, a water corresponding to HOH1 in Fig. 6 was observed in the MBP-A CRD crystal structure interacting with the E185 side chain. Although these waters are seldom observed in complexes with monosaccharides, the combined results of these crystal structures and the behavior of these waters in our simulations support the view that such waters are both integral and highly adaptable structural elements in complexes involving larger carbohydrates.

One remaining question is why the binding constant of the trimannoside to MBP-A is essentially the same as that of simple monosaccharides, such as  $\alpha$ -Me-Man. As mentioned earlier, several reports have indicated that, although MBP-C generally has higher affinity for oligosaccharides than for monosaccharides, MBP-A shows the same affinities for both classes of molecules (Lee and Lee, 1997; Quesenberry et al., 1997; Lee et al., 1999). This has led these workers to postulate that MBP-C has an extended binding surface, perhaps with two binding sites, whereas MBP-A interacts only with a single, terminal sugar residue. In contrast, our NMR and MD results indicate that the trimannoside binds in a conformation in which all three rings can interact with the protein surface: ring I directly with the calcium coordination shell along with a van der Waals contact with H189, ring II via a direct hydrogen bond to K182, and ring III via a water-mediated hydrogen bond to E185 and van der Waals contacts to S145, V199, and I207. Nevertheless, the estimates in Table 6 confirm the results of the binding studies, that the binding affinity for the trimannoside and  $\alpha$ -Me-Man are essentially the same. For the binding affinity to remain constant, any enthalpic gains derived from the additional interactions involving rings II and III must be offset by an entropic cost, and this is also evident in Table 6. The  $\Delta H$  values for the trimannoside are consistently less than that for  $\alpha$ -Me-Man, but so are the values of the  $T\Delta S_{\text{rot}}$  terms. The reduction in  $T\Delta S_{\text{rot}}$  for the trimannoside arose primarily from the freezing of motions of the K182 side chain along with motions of trimannoside hydroxyl groups and waters involved in hydrogen bonds, resulting in a minimal gain in free energy from these additional interactions.

This work was supported by a grant from the National Institutes of Health, GM33225, and a Howard Hughes Medical Institute Predoctoral Fellowship to E.W.S.

We thank Jenny Fredericks, Arikha Moses, and Alanna Schepartz for synthesizing oligonucleotide primers. We thank Karl Hager for fluorescent sequencing of plasmid DNA, and Walt McMurray for performing mass spectrometry. We thank Rob Woods for providing the GLYCAM 97

parameter set and for advice in using AMBER. We also thank Rob Rizzo and Julian Tirado-Rives for helpful discussions involving the MD simulations and Andrew Fowler for computational support.

## REFERENCES

- Al-Hashimi, H. M., P. J. Bolon, and J. H. Prestegard. 2000. Molecular symmetry as an aid to geometry determination in ligand protein complexes. *J. Magn. Reson.* 142:153–158.
- Bax, A., and D. G. Davis. 1985. Practical aspects of two-dimensional transverse NOE spectroscopy. *J. Magn. Reson.* 63:207–213.
- Bolon, P. J., H. M. Al-Hashimi, and J. H. Prestegard. 1999. Residual dipolar coupling derived orientational constraints on ligand geometry in a 53 kDa protein–ligand complex. *J. Mol. Biol.* 293:107–115.
- Bothner-By, A. A., R. L. Stephens, J.-M. Lee, C. D. Warren, and R. W. Jeanloz. 1984. Structure determination of a tetrasaccharide; transient nuclear Overhauser effects in the rotating frame. *J. Am. Chem. Soc.* 106:811–813.
- Brisson, J.-R., and J. P. Carver. 1983. Solution conformation of  $\alpha$ D(1–3)- and  $\alpha$ D(1–6)-linked oligomannosides using proton nuclear magnetic resonance. *Biochemistry.* 22:1362–1368.
- Childs, R. A., T. Feizi, C.-T. Yuen, K. Drickamer, and M. S. Quesenberry. 1990. Differential recognition of core and terminal portions of oligosaccharide ligands by carbohydrate-recognition domains of two mannose-binding proteins. *J. Biol. Chem.* 265:20770–20777.
- Clore, G. M., and A. M. Gronenborn. 1982. Theory and applications of the transferred nuclear Overhauser effect to the study of the conformations of small ligands bound to proteins. *J. Magn. Reson.* 48:402–417.
- Davies, E. J., L.-S. Teh, J. Ordi-Ros, N. Snowden, M. C. Hillarby, A. Hajeer, R. Donn, P. Perez-Pemen, M. Vilardeell-Tarres, and W. E. R. Ollier. 1997. A dysfunctional allele of the mannose binding protein gene associates with systemic lupus erythematosus in a Spanish population. *J. Rheumatol.* 24:485–488.
- De Bruyn, A., and M. Anteunis. 1976. Conformation of the C-5/C-6 fragment of aldohexopyranoses. *Carbohydr. Res.* 47:311–314.
- Doig, A. J., and J. E. Sternberg. 1995. Side-chain conformational entropy in protein folding. *Protein Sci.* 4:2247–2251.
- Drickamer, K. 1988. Two distinct classes of carbohydrate-recognition domains in animal lectins. *J. Biol. Chem.* 263:9557–9560.
- Drickamer, K. 1989. Demonstration of carbohydrate-recognition activity in diverse proteins which share a common primary structure motif. *Biochem. Soc. Trans.* 17:13–15.
- Drickamer, K. 1993.  $\text{Ca}^{2+}$ -dependent carbohydrate-recognition domains in animal proteins. *Curr. Opin. Struct. Biol.* 3:393–400.
- Drickamer, K., M. S. Dordal, and L. Reynolds. 1986. Mannose-binding proteins isolated from rat liver contain carbohydrate-recognition domains linked to collagenous tails. *J. Biol. Chem.* 261:6878–6887.
- Dunitz, J. D. 1994. The entropic cost of bound water in crystals and biomolecules. *Science.* 264:670.
- Ezekowitz, R. A. B. 1998. Genetic heterogeneity of mannose-binding proteins: the Jekyll and Hyde of innate immunity? *Am. J. Hum. Genet.* 62:6–9.
- Ferrin, T. E., C. C. Huang, L. E. Jarvis, and R. Langridge. 1988. The MIDAS display system. *J. Mol. Graph.* 6:13–27.
- Gadjeva, M., S. Thiel, and J. C. Jensenius. 2001. The mannan-binding-lectin pathway of the innate immune response. *Curr. Opin. Immunol.* 13:74–78.
- García-Hernández, E., and A. Hernández-Arana. 1999. Structural bases of lectin–carbohydrate affinities: comparison with protein-folding energetics. *Protein Sci.* 8:1075–1086.
- Garred, P., H. O. Madsen, U. Balslev, B. Hofmann, C. Pedersen, J. Gerstoft, and A. Svejgaard. 1997. Susceptibility to HIV infection and progression of AIDS in relation to variant alleles of mannose-binding lectin. *Lancet.* 349:236–240.
- Garred, P., H. O. Madsen, B. Hofmann, and A. Svejgaard. 1995. Increased frequency of homozygosity of abnormal mannan-binding-protein alleles in patients with suspected immunodeficiency. *Lancet.* 346:941–943.
- Griesinger, C., and R. R. Ernst. 1987. Frequency offset effects and their elimination in NMR rotating-frame cross-relaxation spectroscopy. *J. Magn. Reson.* 75:261–271.
- Hajduk, P. J., D. A. Horita, and L. E. Lerner. 1993. Picosecond dynamics of simple monosaccharides as probed by NMR and molecular dynamics simulations. *J. Am. Chem. Soc.* 115:9196–9201.
- Håkansson, K., and K. B. M. Reid. 2000. Collectin structure: a review. *Protein Sci.* 9:1607–1617.
- Hoppe, H.-J., and K. B. M. Reid. 1994a. Collectins—soluble proteins containing collagenous regions and lectin domains—and their roles in innate immunity. *Protein Sci.* 3:1143–1158.
- Hoppe, H.-J., and K. B. M. Reid. 1994b. Trimeric C-type lectin domains in host defence. *Structure.* 2:1129–1133.
- Ikeda, K., T. Sannoh, N. Kawasaki, T. Kawasaki, and I. Yamashina. 1987. Serum lectin with known structure activates complement through the classical pathway. *J. Biol. Chem.* 262:7451–7454.
- Iobst, S. T., and K. Drickamer. 1996. Selective sugar binding to the carbohydrate recognition domains of the rat hepatic and macrophage asialoglycoprotein receptors. *J. Biol. Chem.* 271:6686–6693.
- Iobst, S. T., M. R. Wormald, W. I. Weis, R. A. Dwek, and K. Drickamer. 1994. Binding of sugar ligands to  $\text{Ca}^{2+}$ -dependent animal lectins. I. Analysis of mannose binding by site-directed mutagenesis and NMR. *J. Biol. Chem.* 269:15505–15511.
- IUPAC-IUB. 1983. Symbols for specifying the conformation of polysaccharide chains. *Eur. J. Biochem.* 131:5–7.
- Kilpatrick, D. C. 1997. Mannan binding protein in sera positive for rheumatoid factor. *Br. J. Rheumatol.* 36:207–209.
- Lee, R. T., and Y. C. Lee. 1997. Difference in binding-site architecture of the serum-type and liver-type mannose-binding proteins. *Glycoconj. J.* 14:357–363.
- Lee, R. T., Y. Shinohara, Y. Hasegawa, and Y. C. Lee. 1999. Lectin-carbohydrate interactions: fine specificity difference between two mannose-binding proteins. *Biosci. Rep.* 19:283–292.
- Loris, R., D. Maes, F. Poortmans, L. Wyns, and J. Bouckaert. 1996. A structure of the complex between concanavalin A and methyl-3,6-di-O-( $\alpha$ -D-mannopyranosyl)- $\alpha$ -D-mannopyranoside reveals two binding modes. *J. Biol. Chem.* 271:30614–30618.
- Lu, J. 1997. Collectins: collectors of microorganisms for the innate immune system. *BioEssays.* 19:509–518.
- Macura, S., and R. R. Ernst. 1980. Elucidation of cross relaxation in liquids by two-dimensional N.M.R. spectroscopy. *Mol. Phys.* 41:95–117.
- McCain, D. C., and J. L. Markley. 1987. Internal motions of the three hydroxymethyl groups in aqueous sucrose. *J. Magn. Reson.* 73:244–251.
- Mrevlishvili, G. M. 1998. Low-temperature heat capacity of biomacromolecules and the entropic cost of bound water in proteins and nucleic acids (DNA). *Thermochim. Acta.* 308:49–54.
- Naismith, J. H., and R. A. Field. 1996. Structural basis of trimannoside recognition by concanavalin A. *J. Biol. Chem.* 271:972–976.
- Ng, K. K.-S., K. Drickamer, and W. I. Weis. 1996. Structural analysis of monosaccharide recognition by rat liver mannose-binding protein. *J. Biol. Chem.* 271:663–674.
- Pearlman, D. A., D. A. Case, J. W. Caldwell, W. S. Ross, T. E. I. Cheatham, D. M. Ferguson, G. L. Seibel, U. C. Singh, P. K. Weiner, and P. A. Kollman. 1995. AMBER 4.1. University of California, San Francisco.
- Petrescu, A. J., S. M. Petrescu, R. A. Dwek, and M. R. Wormald. 1999. A statistical analysis of N- and O-glycan linkage conformations from crystallographic data. *Glycobiology.* 9:343–352.
- Quesenberry, M. S., R. T. Lee, and Y. C. Lee. 1997. Difference in the binding mode of two mannose-binding proteins: demonstration of a selective miniclustering effect. *Biochemistry.* 36:2724–2732.
- Quiocho, F. A. 1989. Protein–carbohydrate interactions: basic molecular features. *Pure Appl. Chem.* 61:1293–1306.
- Rao, V. S., and A. S. Perlin. 1983. A reversal in the order of H-6R and H-6S chemical shifts of some aldohexopyranose derivatives, associated with the acetylation of OH-4 and OH-6 groups: a distinction between 3-

- and 4-linked D-glucose residues in disaccharides. *Can. J. Chem.* 61: 2688–2694.
- Rozwarski, D. A., B. M. Swami, C. F. Brewer, and J. C. Sacchettini. 1998. Crystal structure of the lectin from *Dioclea grandiflora* complexed with core trimannoside of asparagine-linked carbohydrates. *J. Biol. Chem.* 273:32818–32825.
- Sayers, E. W., and J. H. Prestegard. 2000. Solution conformations of a trimannoside from NMR and MD simulations. *Biophys. J.* 79: 3313–3329.
- Sayers, E. W., J. L. Weaver, and J. H. Prestegard. 1998. Hydrogen bonding geometry of a protein-bound carbohydrate from water exchange-mediated cross-relaxation. *J. Biomol. NMR.* 12:209–222.
- Summerfield, J. A. 1993. The role of mannose-binding protein in host defence. *Biochem. Soc. Trans.* 21:473–477.
- Summerfield, J. A., M. Sumiya, M. Levin, and M. W. Turner. 1997. Association of mutations in mannose binding protein gene with childhood infection in consecutive hospital series. *Br. Med. J.* 314: 1229–1232.
- Super, M., J. Lu, S. Thiel, R. J. Levinsky, and M. W. Turner. 1989. Association of low levels of mannan-binding protein with a common defect of opsonization. *Lancet.* 2:1236–1239.
- Thomas, H. C., G. R. Foster, M. Sumiya, D. McIntosh, D. L. Jack, M. W. Turner, and J. A. Summerfield. 1996. Mutation of gene for mannose-binding protein associated with chronic hepatitis B viral infection. *Lancet.* 348:1417–1419.
- Toone, E. J. 1994. Structure and energetics of protein-carbohydrate complexes. *Curr. Opin. Struct. Biol.* 4:719–728.
- Turner, M. W. 1996. Mannose-binding lectin: the pluripotent molecule of the innate immune system. *Immunol. Today.* 17:532–540.
- Turner, M. W. 1998. Mannose-binding lectin (MBL) in health and disease. *Immunobiology.* 199:327–339.
- Weis, W. I., G. V. Crichlow, H. M. K. Murthy, W. A. Hendrickson, and K. Drickamer. 1991a. Physical characterization and crystallization of the carbohydrate-recognition domain of a mannose-binding protein from rat. *J. Biol. Chem.* 266:20678–20686.
- Weis, W. I., K. Drickamer, and W. A. Hendrickson. 1992. Structure of a C-type mannose-binding protein complexed with an oligosaccharide. *Nature.* 360:127–134.
- Weis, W. I., R. Kahn, R. Fourme, K. Drickamer, and W. A. Hendrickson. 1991b. Structure of the calcium-dependent lectin domain from a rat mannose-binding protein determined by MAD phasing. *Science.* 254: 1608–1615.
- Wishart, D. S., C. G. Bigam, J. Yao, F. Abildgaard, H. J. Dyson, E. Oldfield, J. L. Markley, and B. D. Sykes. 1995.  $^1\text{H}$ ,  $^{13}\text{C}$ , and  $^{15}\text{N}$  chemical shift referencing in biomolecular NMR. *J. Biomol. NMR.* 6:135–140.
- Woods, R. J., R. A. Dwek, C. J. Edge, and B. Fraser-Reid. 1995. Molecular mechanical and molecular dynamical simulations of glycoproteins and oligosaccharides. 1. GLYCAM 93 parameter development. *J. Phys. Chem.* 99:3832–3846.
- Wright, C. S., and G. Hester. 1996. The 2.0 Å structure of a cross-linked complex between snowdrop lectin and a branched mannopentaose: evidence for two unique binding modes. *Structure.* 4:1339–1352.